Polyol-assisted efficient hole transfer and utilization at the Si-based photoanode/electrolyte interface

Yaxing Zhao [a], Xiaolei Zhao [a], Kepeng Song [c], Xiaowen Sun [a], Ning Xi [a], Xuedong Zhang [a], Yuanhua Sang [a,*], Hong Liu [a,b,**], Xiaowen Yu [a,*]

[a] *State Key Laboratory of Crystal Materials, Shandong University, Jinan 250100, PR China*
[b] *Jinan Institute of Quantum Technology, Jinan Branch, Hefei National Laboratory, Jinan 250101, PR China*
[c] *School of Chemistry and Chemical Engineering, Shandong University, Jinan 250100, PR China*

ARTICLE INFO

ABSTRACT

The sluggish kinetics of the anodic oxygen evolution reaction significantly restricts the efficiency of silicon (Si)-based photoelectrochemical (PEC) cells. In this study, we employ microfabrication technology to batch-prepare reproducible Si substrates, and develop a facile electrodeposition technique to load high-quality nickel film onto the substrates. Innovatively, we introduce energetically favorable polyols (such as glycerol, propylene glycol, and ethylene glycol) into the electrolyte, resulting in a remarkably low onset potential and a high hole injection efficiency during the PEC oxidation process. Taking glycerol as an example, *in-situ* impendence spectra provide real-time evidence for the accelerated hole transfer and utilization at the photoanode/electrolyte interface in the presence of glycerol. Mechanistic studies further reveal that glycerol undergoes synergistic oxidation mediated by holes and catalysts. Finally, by intergrating a solar thermoelectric generator into a PEC polyol oxidation cell, the self-powered system demonstrates promising potential for producing valuable products solely by harnessing solar energy.

1. Introduction

Over the past few decades, the excessive exploitation of fossil fuels has led to severe environmental pollution and energy crisis. Solar energy, as one of the most abundant natural resources, has emerged as a plausible solution and an effective substitute for fossil fuels. Photoelectrochemical (PEC) water splitting is a promising method for converting solar energy into storable hydrogen fuels [1–3]. Within a PEC cell, the semiconductor material used as the photoelectrode plays a crucial role in determining the efficiency and stability of the devices. Significant progresses have been achieved in searching the appropriate semiconductors following the pioneering work of Fujishima and Honda in 1972, wherein they employed TiO_2 as a photoanode for PEC water splitting [4]. Recently, alternative semiconductors including WO_3 [5], $BiVO_4$ [6–8], α-Fe_2O_3 [9,10], and Silicon (Si) [11–13] have emerged as promising light absorbers for PEC devices. Among these, Si has attracted a great deal of attention due to its narrow band gap (1.12 eV), low cost, and high carrier mobility [14]. Additionally, as the fundamental

material of integrated circuits, Si has driven the advancements of various microfabrication techniques aimed at improving the reproducibility and batch preparation of Si-based devices [15]. Nonetheless, Si is susceptible to photo-corrosion and passivation in aqueous solutions, especially in alkaline environments [16]. Consequently, extensive efforts have been dedicated to engineering protective layers onto the surface of Si to enhance its stability [17]. For instance, the deposition of amorphous TiO_2 through atomic layer deposition (ALD) has proven to be effective in protecting the Si photoanode and enhancing its stability in alkaline media [18]. In addition, transition metal (oxides) layers with catalytic activity can also contribute to the protection of Si [16]. For example, a nickel oxide (NiO_x) layer prepared by radio-frequency sputtering technology [19], a nickel coating deposited through the electron beam evaporation [20], and a cobalt oxide (CoO_x) thin film deposited *via* ALD [21] have demonstrated significant advantages in protecting Si substrates. However, these preparation methods are expensive and complicated, which substantially limits their practical applications. Hence, developing simple, controllable, and cost-effective

processing methods for protective layers on Si substrates is of great importance.

On the other hand, in the PEC water splitting system, the anodic oxygen evolution reaction (OER) is the most energy consumption step due to its sluggish kinetics and high overpotential associated with the four-electron transfer process [22]. Currently, Si-based photoanodes have been extensively studied in the PEC OER system, with a primary focus on regulating interfacial structures, optimizing device architectures, or designing co-catalysts. Liu et al. used amorphous silicon (a-Si) and metal oxides (TiO$_2$) to passivate the dangling bonds on the Si surface and eliminate the metal-induced gap states at the a-Si/Ni interface. The resulting Si photoanode exhibited an ultra-low interfacial recombination rate, leading to a small onset potential of 0.85 V vs. RHE for PEC OER [23]. In addition, significant efforts have been directed towards introducing high work function co-catalysts to increase the barrier height of the Si photoanode, aming to facilitate carriers separation and transfer during PEC OER [24,25]. Hill et al. prepared a n-Si/SiO$_x$/Co/-CoOOH photoanode for PEC OER and found that the significant increase in barrier height led to an enhanced photovoltage of 360 mV [26]. Furthermore, Luo et al. modified the Si-based photoanode with a Ni/NiO$_x$/NiOOH layer, resulting in the achievement of a low onset potential of 0.85 V vs. RHE for OER [27]. Although great progresses have been achieved in reducing the onset potential and improving the carriers transfer of Si photoanodes for PEC OER, it still remains challenging to overcome the limiting overpotential and inefficient hole utilization associated with OER. Furthermore, the impact of the electrolyte on the PEC oxidation reaction has received limited attention. In reality, the electrolyte plays a crucial role in modifying the behavior of charge carriers at the electrode/electrolyte interface, which will significantly impact the energy conversion efficiency of the Si photoanodes [28]. Therefore, there is an urgent need to comprehend the influence of the electrolyte on the dynamics of charge carriers and to develop advanced technologies that facilitate the evaluation of charge carrier behaviors, ultimately aiming to improve PEC efficiency.

Here, we utilize microfabrication technology to batch-prepare reproducible Si substrates. Additionally, we develop a facile, cost-effective, and controllable electroplating method for depositing Ni nanoparticles (NPs) onto the np$^+$-Si surface, serving as a protective and catalytic layer. The resulting np$^+$-Si/SiO$_x$/Ni device exhibits enhanced PEC performance in a 1.0 M KOH electrolyte upon addition of energetically favorable glycerol molecules. Specifically, the onset potential is negatively shifted by 0.22 V, and the hole injection efficiency (at 1.23 V vs. RHE) increases by 101% in the presence of glycerol compared to pure KOH electrolyte. The *in-situ* impedance spectra offer real-time insights into the enhanced efficiencies of transfer and utilization at the photoanode/electrolyte interface when glycerol is present. Furthermore, mechanistic studies uncover the direct and synergistic oxidation mechanisms of glycerol during the PEC oxidation process. The impact of glycerol on PEC performance can extend to other active diols, such as propylene glycol and ethylene glycol, reinforcing the pivotal role of the electrolyte in faciliating the separation and transfer of photogenerated charge carriers at the photoanode/electrolyte interface. Finally, the integration of a solar thermoelectric generator into a self-powered PEC polyol oxidation system showcases promising potential for producing value-added products by solely relying on renewable solar energy.

2. Experimental section

2.1. Preparation of the np$^+$-Si/SiO$_x$/Ni photoanode

Before the electrodeposition of Ni NPs onto the np$^+$-Si substrate, Si substrate was subjected into the buffered oxide etch (BOE) solution for 15 s to remove the native SiO$_2$. Then the etched Si surface was washed with deoxygenated water and quickly dried under nitrogen flow. Subsequently, the np$^+$-Si substrate was immersed into nitrogen-purged aqueous plating solution containing 0.27 M NiSO$_4$·6 H$_2$O, 0.012 M L-

histidine, and 0.12 M H$_3$BO$_3$ for the electrodeposition of Ni NPs. The electrodeposition process was carried out in a three-electrode system with the encapsulated np$^+$-Si substrate served as the working electrode, a platinum slice (1 × 1 cm^2) as the counter electrode and a saturated calomel electrode (SCE, with saturated KCl solution) acted as the reference electrode. A constant potential of -1.33 V vs. RHE was applied to the working electrode at room temperature for various durations, resulting in the deposition of Ni layers with different charges (10, 20, 30, and 40 mC cm^{-2}).

2.2. Characterizations

The atomic force microscopy (AFM) topography images were obtained using a Bioscope Resolve atomic force microscope (Bruker) in the tapping mode. Scanning electron microscope (SEM) images were obtained using Geimini 500 scanning electron microscopy (Carl Zeiss, Germany). The grazing incidence X-ray diffraction (GIXRD) pattern was recorded on a X Pert Powder X-ray diffractometer (PANalytical, Netherlands) with Cu Kα radiation (λ = 0.15418 nm). X-ray photoelectron spectra (XPS) upon different ion milling depths were performed on a Thermo Scientific K-Alpha photoelectron spectrometer with Al Kα as radiation source (hυ = 1486.60 eV), 400 μm spot size with a pass energy of 100 eV for full spectra and 50 eV for high-resolution spectra. The XPS peaks were fitted using XPSpeak41 software. The transmission electron microscopy (TEM) specimen of the np$^+$-Si/SiO$_x$/Ni photoanode sample was thinned by focused ion beam (FIB, Helios G4 UC) technique and the surface of the sample was protected by electron beam deposited Pt and sputtered Pt. The FIB-prepared specimen was analyzed by TEM and scanning transmission electron microscopy (Spectra 300, Thermo Scientific) with an equipment of energy dispersion spectroscopy (EDS).

2.3. Synthesis of carbon nanoparticles (CNPs)

The CNPs were grown *in-situ* on the surface of the thermoelectric generator (TEG1–241–1.4–1.2, 5.5 cm × 5.5 cm) by igniting paraffin candles. After the flame was stable, the hot-side of the commercial solar thermoelectric generator (STEG) was uniformly exposed to the flame to ensure the loading of CNPs. The wick of the candle was positioned parallel to the hot-side surface, with a distance of 2 cm. The average baking time was approximately 2 s cm^{-2}.

2.4. PEC measurements

All the PEC measurements were performed on a electrochemical workstation (CHI660E, Shanghai Chenhua Instrument Company) at room temperature in a standard three-electrode setup within a quartz cell. The np$^+$-Si/SiO$_x$/Ni photoanode was used as the working electrode, a Pt slice as the counter electrode, and a SCE as the reference electrode. The 1.0 M KOH aqueous solution with or without 0.1 M glycerol was used as the electrolyte. A Xenon lamp (CEL-S500-T5, Beijing Aulight Technology Co., Ltd.) with an AM 1.5 G filter was used as the light source with an intensity of 100 mW cm^{-2}, simulating as 1-sun illumination. All measured potentials were converted to the reversible hydrogen electrode (RHE) reference using the following equation: E$_{RHE}$ = E$_{SCE}$ + 0.244 + 0.059 pH, where E$_{RHE}$ is the potential referred to RHE, and E$_{SCE}$ is the measured potential against SCE reference electrode. The LSV profiles were collected at a scan rate of 10 mV s^{-1} with a potential ranging from 0.25 to 2.10 V vs. RHE under 1-sun illumination or in the dark. The chronoamperometric spectra were collected at 0.89 V vs. RHE under chopped light illumination with a time interval of 5 s. The electrochemical impedance spectra (EIS) were performed at a series of potentials ranging from 0.54 to 1.14 V vs. RHE from the frequency range of 10^{-2} to 10^5 Hz with a 5 mV AC amplitude under light illumination. The EIS data was fitted using Zview software.

2.5. High-performance liquid chronometry (HPLC) measurements

The products from the oxidation of several polyols were collected in a two-electrode system after 1 h operation in the self-powered PEC system. Typically, 1 mL of product solution was collected and neutralized by 1 mL 0.5 M H_2SO_4 before analyzing by HPLC (Shimadzu, LC 2050 C). The HPLC was equipped with a Micro-Guard cation H^+ cartridge (4.6 × 30 mm), a Bio-Rad Aminex HPX-87 H column (7.8 × 300 mm), and a Shodex Sugar SH1011 column (8 × 300 mm) in series. All the products were analyzed both by photodiode array detector (PDA at 50 °C) and refractive index detector (RID-20A at 30 °C).

3. Results and discussion

3.1. Preparation of Si substrate

The phosphorous-doped n-type monocrystalline Si <100> with a resistivity of 0.05 – 0.20 Ω cm and a thickness of 450 μm was selected as the substrate for the fabrication of buried junction Si photoanode. The preparation processes are schematically illustrated in Fig. 1. First, a 300 nm insulating SiO_2 layer was thermally grown on the freshly etched Si substrate. Then, a thin layer of photoresist was evenly distributed onto

the surface of the SiO_2 layer by spin coating and followed by soft baking to evaporate the solvent and promote the cross-linking/polymerization of the photoresis. After that, the wafer was exposed to UV–visible light under a photomask. The exposure process initiated a chemical reaction in the photosensitive agents present in the photoresist, making the chemical composition of the irradiated region changed. The wafer then underwent a developing process after the exposure. The developer solution selectively dissolved and removed the regions of photoresist that were exposed to UV–visible light, finally exposing the underlying SiO_2 layer in those regions. The remaining photoresist formed a patterned mask on the surface of the SiO_2 layer. Successively, the exposed SiO_2 layer was etched by hydrofluoric acid (HF) until the underlying Si surface was exposed. While the unexposed SiO_2 layer functions as a pattern, ensuring a constant area for the exposed Si window. The remaining photoresist on the SiO_2 layer was removed by acetone and ethanol. Subsequently, the exposed Si regions were implanted with 4×10^{15} cm^2 dose of boron at 33 keV. Then, the wafer was subjected to an annealing process for 45 min at 950 °C to activate the boron atoms and allow them to diffuse into the Si lattice, resulting in the formation of a well-defined buried junction within the Si crystal (denoted np^+-Si). Followingly, 200 nm layer of aluminum (Al) was deposited onto the backside of the Si substrate through magnetron sputtering to form the Ohmic contact. The
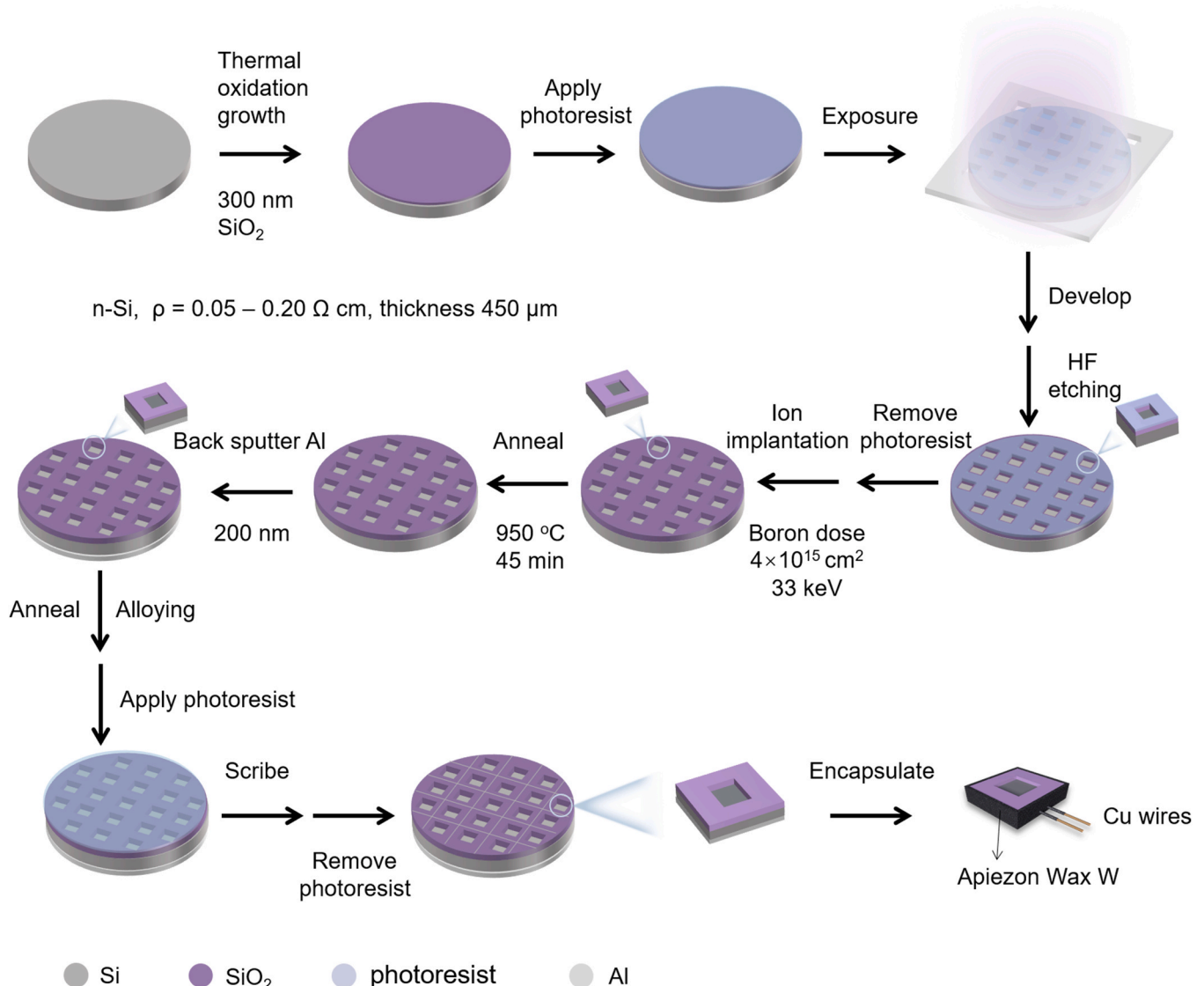

Fig. 1. Schematic diagrams for the preparation of Si substrate through microfabrication process.

wafer was then annealed at 430 °C for 30 min to promote the alloying between Al and Si, ultimately improving the electrical conductivity and adhesion of the back contact. Following, a thin layer of photoresist was applied on the front side of the wafer once again to act as a protective mask to prevent the contamination during the subsequent scribing process. After scribing, each small slice of Si with a size of $0.80 \times 0.80 \ cm^2$ can be directly utilized as an individual device.

Finally, the individual Si slice was encapsulated for subsequent modification. Before encapsulating, the Si slices were washed with acetone, ethanol, and isopropanol for 5 min successively through sonication and then dried by blowing N_2 gas. Copper wires were attached to the backside of Al with silver paste. The edges and backside of Si slice were wrapped with Apiezon Wax W (dissolved in hexane) to prevent the conductive parts contacting with electrolytes. More details for encapsulating Si device can be found in Fig. S1.

3.2. Preparation and optimization of the np^+-Si/SiO$_x$/Ni photoanode

Ni was electrodeposited onto the np^+-Si surface in a three-electrode setup, as illustrated in Fig. 2a. In this setup, the encapsulated np^+-Si substrate served as the working electrode, a platinum slice and a SCE were used as the counter and reference electrodes, respectively. Before electroplating, the np^+-Si electrode was subjected to immerse into BOE solution for 15 s to remove the natural SiO_2 layer on the surface of the Si window. Then the etched Si surface was quickly washed with deoxygenated deionized water and dried by blowing N_2 gas. Subsequently, the np^+-Si electrode was immersed into the deoxygenated plating solution, leading to formation of a thin and loose layer of silicon oxide (SiO_x) on the surface, which can serve as an effective tunneling layer to promote the transfer of photogenerated charge carriers [26,29].

The plating solution consists of 0.27 M NiSO$_4$·6H$_2$O, 0.012 M L-histidine, and 0.12 M H$_3$BO$_3$. Among which, NiSO$_4$·6H$_2$O serves as the source of Ni ions. H$_3$BO$_3$ is used to adjust the pH of the plating solution. The pH of the electroplating solution was measured to be 3.90, making the imidazole side chain (N$_i$) and terminal amino group (N$_t$) of the L-histidine positively charged due to the adsorption of proton (H$^+$), and the carboxyl group (O$_c$) negatively charged due to the loss of proton [30]. This enables L-histidine to form complexes with the Ni ions, ensuring their uniform coating on the surface of Si during the electrodeposition process. In the complexes, Ni atoms serve as the central atoms to provide six empty orbitals, L-histidine or H$_2$O acts as the ligand to provide single electrons [31]. The interaction between Ni^{2+} cations and L-histidine occurs through N$_i$-Ni-O$_c$/N$_t$ bonds [30]. One Ni^{2+} cation forms a complex with two L-histidine molecules by coordinating with two N atoms from N$_i$ and two N atoms from N$_t$, as well as two O atoms from O$_c$. Alternatively, it can coordinate with one L-histidine molecule and three H$_2$O molecules by interacting with one N atom from N$_i$, one N atom from N$_t$, one O atom from O$_c$, and three O atoms from hydroxyl groups of H$_2$O (see Fig. 2a). During the electrodeposition process, when a reduction current is applied, the complexes dissociate and accept electrons, resulting in the reduction of Ni^{2+} complexes to Ni NPs [32]. The chronoamperometric curve, as shown in Fig. S2, reflects the real-time state of the nucleation and growth of Ni NPs during the electrodeposition process [26].

The deposited Ni NPs film on the Si surface can not only serve as a protective layer to inhibit the underlying Si substrate from corrosion, but also act as a catalyst layer to enhance the catalytic performance of the photoanode. By controlling the depositing charge, which is achieved by adjusting the time during the deposition, the amount, thickness, and size of the Ni NPs can be varied. That directly impacts the OER
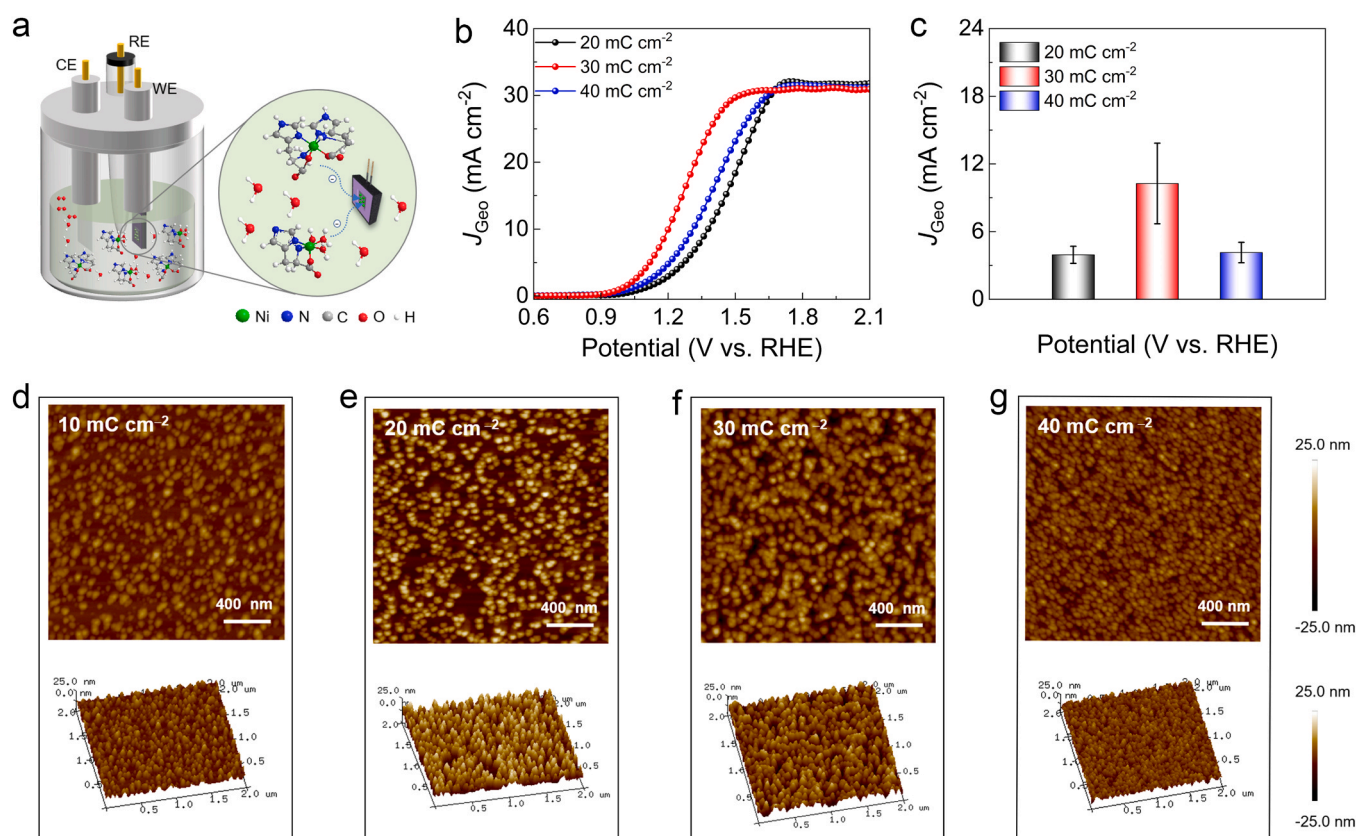

Fig. 2. Optimization of np^+-Si/SiO$_x$/Ni photoanode. (a) A schematic diagram for the electrodeposition of Ni on the np^+-Si electrode. (b) Typical LSV profiles of the np^+-Si/SiO$_x$/Ni photoanodes (Ni deposited at different charges) in 1.0 M KOH at a scan rate of 10 mV s^{-1} under 1-sun illumination (AM 1.5, 100 mW cm^{-2}). (c) Comparison of current densities at various photoanodes recorded at 1.23 V (vs. RHE) averaged over 3 parallel experiments. (d-g) AFM height images and 3D surface profiles of electrodeposited Ni film on np^+-Si at different charges: (d) 10, (e) 20, (f) 30, and (g) 40 mC cm^{-2}.

performance of the np$^+$-Si/SiO$_x$/Ni photoanode. The linear scan voltammetry (LSV) profiles were conducted in 1.0 M KOH solution under 1-sun illumination to evaluate the OER performance of various photoanodes, as shown in Fig. 2b. The onset potentials (defined as the potential at 1.00 mA cm^{-2} [33]) are 1.08, 0.98, and 1.02 V (vs. RHE) for the np$^+$-Si/SiO$_x$/Ni electrodes deposited under 20, 30, and 40 mC cm^{-2}, respectively. When the electrodeposition charge is controlled to 30 mC cm^{-2}, the np$^+$-Si/SiO$_x$/Ni photoanode exhibited the smallest onset potential (0.98 V vs. RHE), and the lowest potential (1.59 V vs. RHE) to reach the saturation current density of 31.62 mA cm^{-2}. While for the other two photoanodes, the potentials are 1.71 and 1.68 V (vs. RHE) respectively to reach their saturated current densities. In addition, the current densities of the various photoanodes at 1.23 V (vs. RHE) were compared over three parallel experiments, see Fig. 2c. When the depositing charge is 30 mC cm^{-2}, the corresponding np$^+$-Si/SiO$_x$/Ni photoanodes have the highest average current density of 10.26 $\pm$ 3.57 mA cm^{-2}. The above results indicated that 30 mC cm^{-2} is the optimized deposition condition for the np$^+$-Si/SiO$_x$/Ni photoanode.

To further elucidate the influence of deposition charge on the morphology of Ni NPs film, the AFM images of the photoanodes deposited under different charges (10, 20, 30, and 40 mC cm^{-2}) were analyzed, see Fig. 2d-g. AFM images showed that the surface of Ni film is composed of un-coalesced islands, which may be due to that the growth of Ni film obeys a Volmer-Weber growth model [34]. When the deposition charge is 10 mC cm^{-2}, the Ni NPs film has the minimum coverage that is not sufficient to protect the underlying Si substrate (Fig. 2d), thus making the surface quickly corrosive under alkaline media. With increasing the electroplating charge from 10 to 30 mC cm^{-2}, the coverage and roughness of Ni NPs are increased and the continuity of the film is enhanced. The Ni film formed at 30 mC cm^{-2} has a suitable coverage (Fig. 2f), which can both protect underlying Si substrate and provide sufficient active sites for the catalytic reaction. In addition, the Ni NPs film deposited at 30 mC cm^{-2} also exhibited large-area uniformity, as shown in SEM images (Fig. S3). Therefore, unless otherwise mentioned, the np$^+$-Si/SiO$_x$/Ni photoanode referred following all indicate that Ni film was deposited at 30 mC cm^{-2}.

3.3. Characterization of the np$^+$-Si/SiO$_x$/Ni photoanode

To confirm the component and structure of the electrodeposited Ni film, the GIXRD pattern was tested (Fig. 3a), which exhibited three distinct diffraction peaks at $2\theta = 44.50°$, $51.80°$ and $76.40°$, corresponding to the (111), (200), and (220) crystal planes of cubic Ni (JCPDS card no. 04–0850) [35,36]. The GIXRD results indicated that the
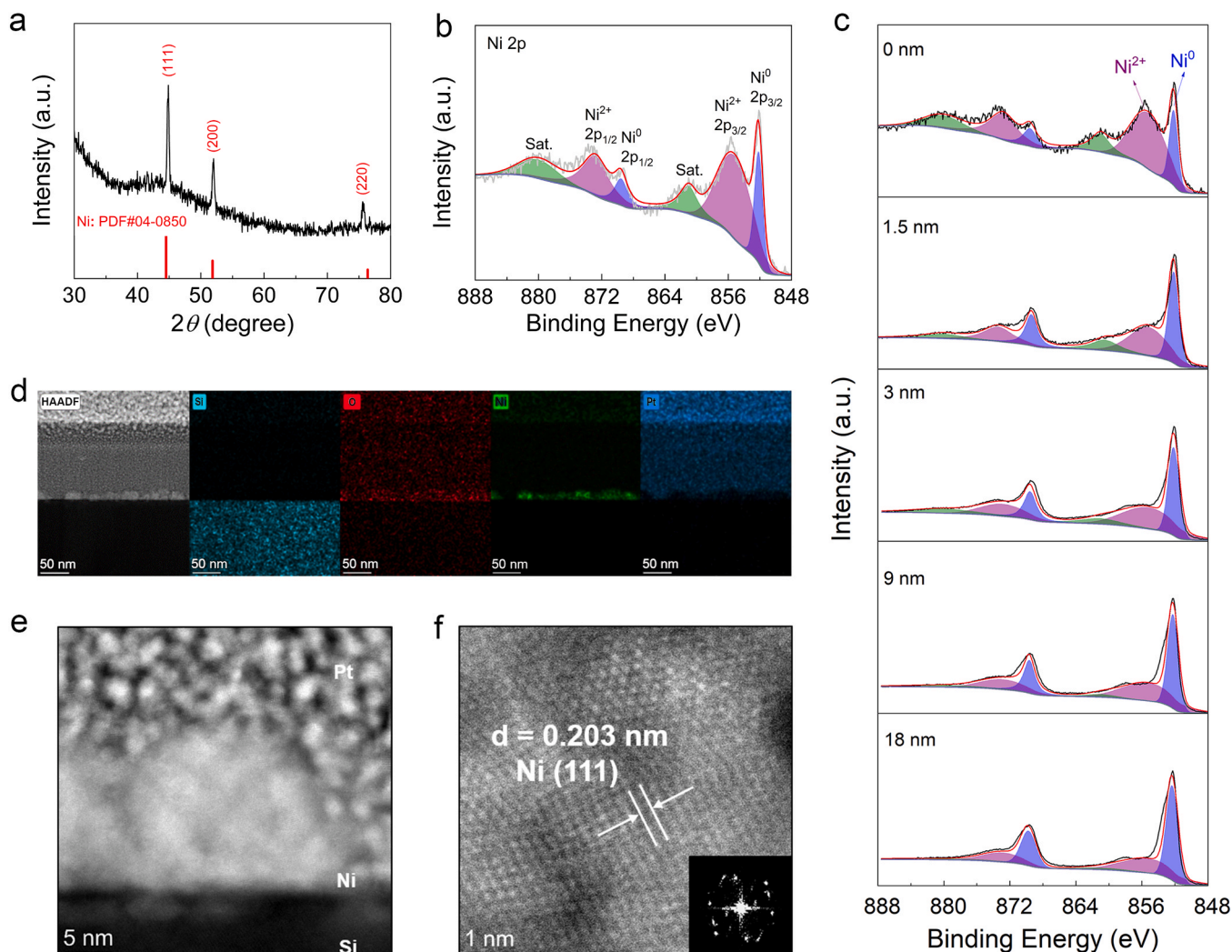

Fig. 3. Characterization of deposited Ni NPs film. (a) GIXRD pattern of the np$^+$-Si/SiO$_x$/Ni photoanode. (b) Ni 2p XPS spectra of surface Ni layer on the np$^+$-Si/SiO$_x$/Ni photoanode. (c) Ni 2p XPS spectra of the np$^+$-Si/SiO$_x$/Ni photoanode upon different ion milling depths. (d) Cross-sectional STEM image of the np$^+$-Si/SiO$_x$/Ni photoanode and the corresponding EDS mappings of Si, O, Ni, and Pt elements. (e) HRTEM image of the cross-sectional np$^+$-Si/SiO$_x$/Ni photoanode. (f) HRTEM image of an individual Ni NP.

surface deposited Ni NPs film is polycrystalline Ni phase crystallized in the space group of $Fm\bar{3}m$.

The elemental composition and chemical bonding states of the surface Ni film at the np^+-Si/SiO$_x$/Ni photoanode were characterized by XPS, see Fig. 3b and Fig. S4. The high-resolution Ni 2p XPS spectrum can be deconvoluted into six peaks. The peaks at binding energies of 852.15 and 869.45 eV, with a shake-up energy difference of 17.30 eV, can be attributed to the metallic Ni^0 2p$_{3/2}$ and 2p$_{1/2}$ doublets, respectively. The peaks located at 855.20 and 872.80 eV, with a binding energy difference of 17.60 eV, can be assigned to Ni^{2+} 2p$_{3/2}$ and 2p$_{1/2}$ doublets, respectively [37]. The presence of these two peaks may derive from the oxidation of metallic Ni NPs in the air or the formation of Ni(OH)$_2$ from the plating solution. In addition, the fitting peaks at 861 and 880 eV correspond to the satellite peaks of Ni 2p$_{3/2}$ and Ni 2p$_{1/2}$, respectively.

Furthermore, the XPS depth profiling experiments were carried out at different Ar ion milling depths to further ascertain the surface composition of the prepared np^+-Si/SiO$_x$/Ni photoanode (Fig. 3c). The high-resolution Ni 2p XPS spectra revealed that the proportion of Ni^{2+} gradually decreased and metallic Ni increased as the etching depth increased from 0 to 18 nm. For the respective etching depths of 0, 1.5, 3, 9, and 18 nm, the Ni^{2+}/Ni^0 ratios changed from 2.85, 1.50, 1.13, 0.92, to 0.69. The shift towards a higher proportion of metallic Ni suggests that the electrodeposited Ni NPs film primarily consists of metallic Ni, with slight surface oxidation.

To observe the morphology of the cross-section of the photoanode, the FIB technique was applied to thin the sample and load it onto the copper grid. Prior to the FIB process, Pt was deposited on the Ni film surface to prevent damage to the Ni surface. The cross-sectional
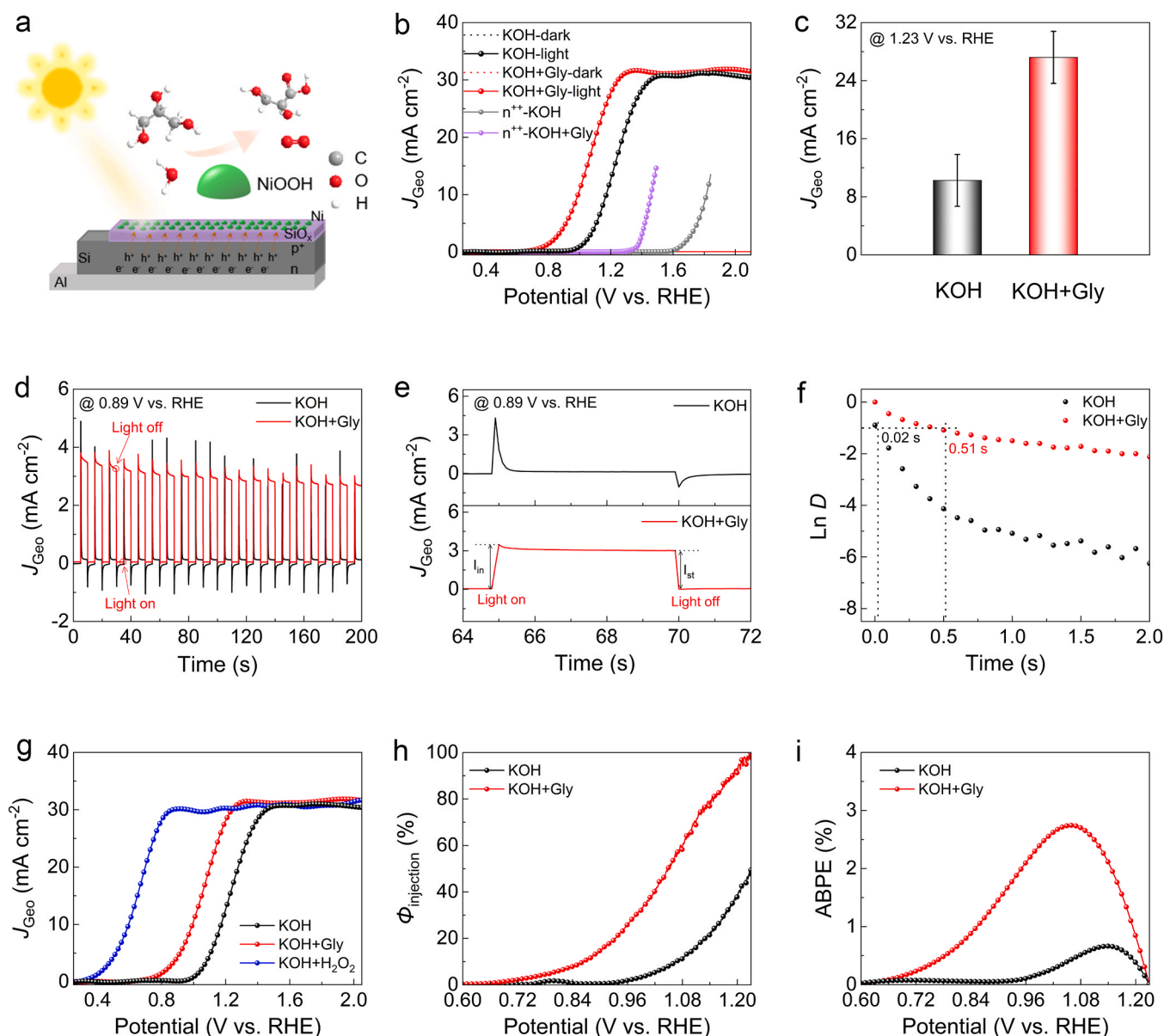

Fig. 4. PEC performance. (a) Schematic illustration of the structure of np^+-Si/SiO$_x$/Ni photoanode for PEC OER/GOR. (b) LSV profiles of the np^+-Si/SiO$_x$/Ni photoanode in 1.0 M KOH with or without 0.1 M glycerol under 1-sun illumination. (c) Comparison of current density at 1.23 V (vs. RHE) of the np^+-Si/SiO$_x$/Ni photoanode for OER and GOR averaged over three parallel experiments. (d) The chopped chronoamperometry profiles of the np^+-Si/SiO$_x$/Ni photoanode at 0.89 V (vs. RHE) in 1.0 M KOH with or without 0.1 M glycerol. (e) Comparison of transient photocurrent density responses at 0.89 V (vs. RHE). (f) The plot of the lnD as a function of time for calculating the transient time constant (τ_D). (g) LSV profiles of the np^+-Si/SiO$_x$/Ni photoanode in 1.0 M KOH with 0.5 M H$_2$O$_2$ under 1-sun illumination compared to 1.0 M KOH with or without 0.1 M glycerol. (h) Charge injection efficiencies ($\Phi_{injection}$) and (i) applied bias photon-to-current efficiencies (ABPE) of the np^+-Si/SiO$_x$/Ni photoanode for OER and GOR.

structure of the photoanode was examined by scanning transmission electron microscopy (STEM). The EDS mapping images in Fig. 3d indicate the presence and uniform distribution of Si, O, Ni, and Pt elements across the np^+-Si/SiO$_x$/Ni photoanode. The high-resolution transmission electron microscopy (HRTEM) image of the cross-sectional np^+-Si/SiO$_x$/Ni photoanode, displayed in Fig. 3e, further confirms that the Ni NPs with an average size of 16 nm are discontinuously deposited as a thin island film on the Si surface, that would effectively reduce the reflection of the incident light [29]. The HRTEM image also clearly reveals that a thin and amorphous SiO$_x$ layer with a thickness of 1.8 nm is formed between the Ni island film and Si substrate. This SiO$_x$ layer can serve as a tunneling layer to promote the transfer of charge carriers and also act as a protective layer to prevent the Si substrate from electrolyte/photo corrosion [38]. In Fig. 3f, the lattice fringe with a d-spacing of 0.203 nm is observed, corresponding to the characteristic (111) lattice plane of Ni, which is in consistent with the GIXRD result.

3.4. PEC performance of the np^+-Si/SiO$_x$/Ni photoanode

The PEC performance of the np^+-Si/SiO$_x$/Ni photoanode was evaluated in an electrolyte of 1.0 M KOH with or without 0.1 M glycerol under 1-sun illumination, using a standard three-electrode system within a quartz cell. For comparison, the heavily As-doped n-type Si deposited with Ni (n^{++}-Si/SiO$_x$/Ni, $\rho = 0.001 - 0.002\ \Omega$ cm, thickness of 450 μm) was also prepared and tested under the identical conditions. A schematic illustration of the structure of np^+-Si/SiO$_x$/Ni photoanode is depicted in Fig. 4a. In this photoanode, Si substrate acts as the light absorber and generates electrons and holes under excitation. The p-n junction established by doping boron atoms acts as an internal electric filed to promote the separation of photogenerated electrons and holes [39]. The SiO$_x$ layer formed during electrodeposition process can reduce the Fermi level pinning effect [26,29]. Upon the action of internal electric field and the applied positive bias, photogenerated holes can be effectively separated and transferred through the SiO$_x$ layer [40,41]. The surface Ni NPs film acts as both the protective and catalytic layer for the Si substrate.

Fig. 4b shows typical LSV profiles of the np^+-Si/SiO$_x$/Ni photoanode and the n^{++}-Si/SiO$_x$/Ni electrode under dark or illumination conditions. The current densities measured in the dark condition for the np^+-Si/SiO$_x$/Ni electrode are all close to zero in 1.0 M KOH with or without 0.1 M glycerol over the applied potential range, indicating that these electrodes are well encapsulated without noticeable current leakage. The saturation current densities for the np^+-Si/SiO$_x$/Ni photoanode under 1-sun illumination in 1.0 M KOH with or without 0.1 M glycerol are around 31.6 mA cm^{-2}. The sharp current difference between the light and dark conditions indicates that the current under light irradiation mainly comes from the contribution of photogenerated charge carriers. The np^+-Si/SiO$_x$/Ni photoanode demonstrates an onset potential of 0.98 V (vs. RHE) for OER. In the presence of glycerol, the np^+-Si/SiO$_x$/Ni photoanode exhibits an extremely low onset potential of 0.76 V (vs. RHE) for glycerol oxidation reaction (GOR), which is negatively shifted by 0.22 V compared to OER and shifted by 0.47 V compared to the equilibrium oxidation potential of water (1.23 V vs. RHE), indicating that glycerol molecule is more easily oxidized than water. In addition, the n^{++}-Si/SiO$_x$/Ni electrode was performed for OER and GOR in dark to evaluate the electrocatalytic performance of the surface catalyst and the photovoltage of the photoanode. Here, the photovoltage is defined as the potential difference between the np^+-Si/SiO$_x$/Ni photoanode in light and the n^{++}-Si/SiO$_x$/ Ni electrode in dark to reach a current density of 1.00 mA cm^{-2} [42]. The photovoltages of the np^+-Si/SiO$_x$/Ni photoanode for OER and GOR were calculated to be 620 and 600 mV, respectively. Furthermore, the current densities of the photoanode for OER and GOR at a potential of 1.23 V (vs. RHE) were compared over three parallel photoanodes (see Fig. 4c), which are 10.26 $\pm$ 3.57 and 27.19 $\pm$ 3.59 mA cm^{-2}, respectively, further confirming the favorable oxidation kinetics of glycerol than water.

To study the property difference of the photogenerated charge carriers at the np^+-Si/SiO$_x$/Ni photoanode in the presence or absence of glycerol, chopped photocurrent measurements were performed by chronoamperometry at a constant potential of 0.89 V (vs. RHE), as shown in Fig. 4d. The fast instantaneous photocurrent response when light is on/off indicates that the photoanode is sensitive to light illumination. The steady-state current in the electrolyte containing glycerol (3.06 mA cm^{-2}) is significantly higher than that without glycerol (0.16 mA cm^{-2}), indicating that the photogenerated holes can be more effectively utilized in the presence of glycerol. The relationship between the spike of initial photocurrent (I_{in}) and steady-state photocurrent (I_{st}) is associated with the utilization of photogenerated holes (Fig. 4e). I_{in} represents the accumulation of photogenerated holes. However, over time, the photocurrent starts to decay and eventually reaches a steady-state (I_{st}) as the rate of charge generation and recombination reach an equilibrium [43]. To quantitatively analyze the recombination behavior of the photogenerated charge carriers, we calculated the transient time constant (τ_D). This parameter was obtained by plotting a logarithmic curve of the parameter D using the equation [44]

$$D = \frac{I_t - I_{st}}{I_{in} - I_{st}} \tag{1}$$

where I_t represents the photocurrent at a specific time (t). The τ_D is defined when $\ln D = -1$. As illustrated in Fig. 4f, the values of τ_D for the np^+-Si/SiO$_x$/Ni photoanode in 1.0 M KOH in absence and presence of 0.1 M glycerol were measured to be 0.02 and 0.51 s, respectively. The significant increase in τ_D when glycerol is present indicates a lower charge carrier recombination rate during the GOR process. This suggests that glycerol can effectively reduce the recombination of photogenerated electron-hole pairs and enhance the utilization of charge carriers at the photoanode/electrolyte interface.

The photoanode/electrolyte interface has a significant influence on the PEC performance, particularly in terms of the injection of photogenerated charge carriers. Herein, H$_2$O$_2$ was introduced as a hole scavenger to study the np^+-Si/SiO$_x$/Ni photoanode/electrolyte interface (Fig. 4g and Fig. S5a). Under 1-sun illumination, the photoanode exhibits an onset potential of 0.36 V (vs. RHE) in 1.0 M KOH solution with 0.5 M H$_2$O$_2$. The transient current disappears in the applied potential range (Fig. S5b), indicating that the oxidation of H$_2$O$_2$ rapidly consumes the photogenerated holes arrived at the photoanode surface, thus effectively inhibiting the recombination of photogenerated electrons and holes at the photoanode/electrolyte interface. The hole injection efficiency ($\phi_{injection}$) of the photoanode can be calculated through dividing the current density of OER or GOR by the current density for H$_2$O$_2$ oxidation, see Fig. 4h. Throughout the entire studied potential range, the $\phi_{injection}$ at the np^+-Si/SiO$_x$/Ni photoanode in the presence of glycerol is significantly higher than that without glycerol. In particular, at 1.23 V (vs. RHE), the $\phi_{injection}$ is around 49.50% in KOH electrolyte, which can be greatly improved to approximately 99.74% when glycerol is added. The above results indicate that the photogenerated holes accumulated at the electrode/electrolyte interface are more efficiently injected into the electrolyte when participating in GOR.

The applied bias photon-to-current efficiency (ABPE) of the np^+-Si/SiO$_x$/Ni photoanode in KOH in absence or presence of glycerol was calculated based on its LSV profile (see Fig. 4i). The maximum ABPE in 1.0 M KOH with 0.1 M glycerol was measured to be 2.74%, which is substantially higher than that in pure 1.0 M KOH electrolyte (0.66%). The improved ABPE in the presence of glycerol is attributed to the more negative onset potential and the higher current density before 1.23 V (vs. RHE) for GOR, further confirming the significant influence of electrode/electrolyte interface on the PEC performance.

3.5. Insight into the dynamics of the photogenerated charge carriers at the np⁺-Si/SiOx/Ni photoanode

The composition of electrolyte in a PEC system has a significant impact on the photovoltaic properties of the photoanode, particularly by affecting the dynamics of carrier transfer [45]. To investigate the charge transfer characteristics of the np^+-Si/SiO$_x$/Ni photoanode, the EIS were measured under 1-sun illumination at various applied potentials in 1.0 M KOH electrolyte with or without 0.1 M glycerol. Fig. 5a depicts the typical Nyquist plots of the np^+-Si/SiO$_x$/Ni photoanode at 0.94 V (vs. RHE) in these two electrolytes. The inset in Fig. 5a presents the equivalent circuit model used to simulate the EIS response, where R_s is the solution resistance. R_1 is the bulk charge transfer resistance, corresponding to the magnitude of the first semicircle. C_1 is the double layer capacitance associated with the charge transfer in the bulk photoanode. R_2 is the interfacial charge transfer resistance between electrode and electrolyte, corresponding to the magnitude of the second semicircle. C_2 is the double layer capacitance associated with the charge transfer at the photoanode/electrolyte interface. The R_2 values of the np^+-Si/SiO$_x$/Ni photoanode for OER and GOR were measured to be 145.08 and 20.84 Ω cm^2, respectively. The significantly reduced R_2 in the presence of glycerol implies that glycerol can greatly facilitate the charge transfer kinetics at the photoanode/electrolyte interface. The Nyquist plots under other potentials are shown in Fig. S6 and S7 and the simulated resistance values are listed in Table S1.

The relationship between R and the applied potential in both electrolytes was further plotted in Fig. 5b. At lower potentials (< 0.84 V vs. RHE), R_1 remains nearly constant and its value is much smaller than R_2 in both electrolytes, indicating the rapid bulk charge transfer kinetics from the Si substrate to the catalyst layer. In this regard, the primary limiting factor affecting the reaction kinetics is the interfacial charge transfer from the catalyst layer to the electrolyte (indicated by the high
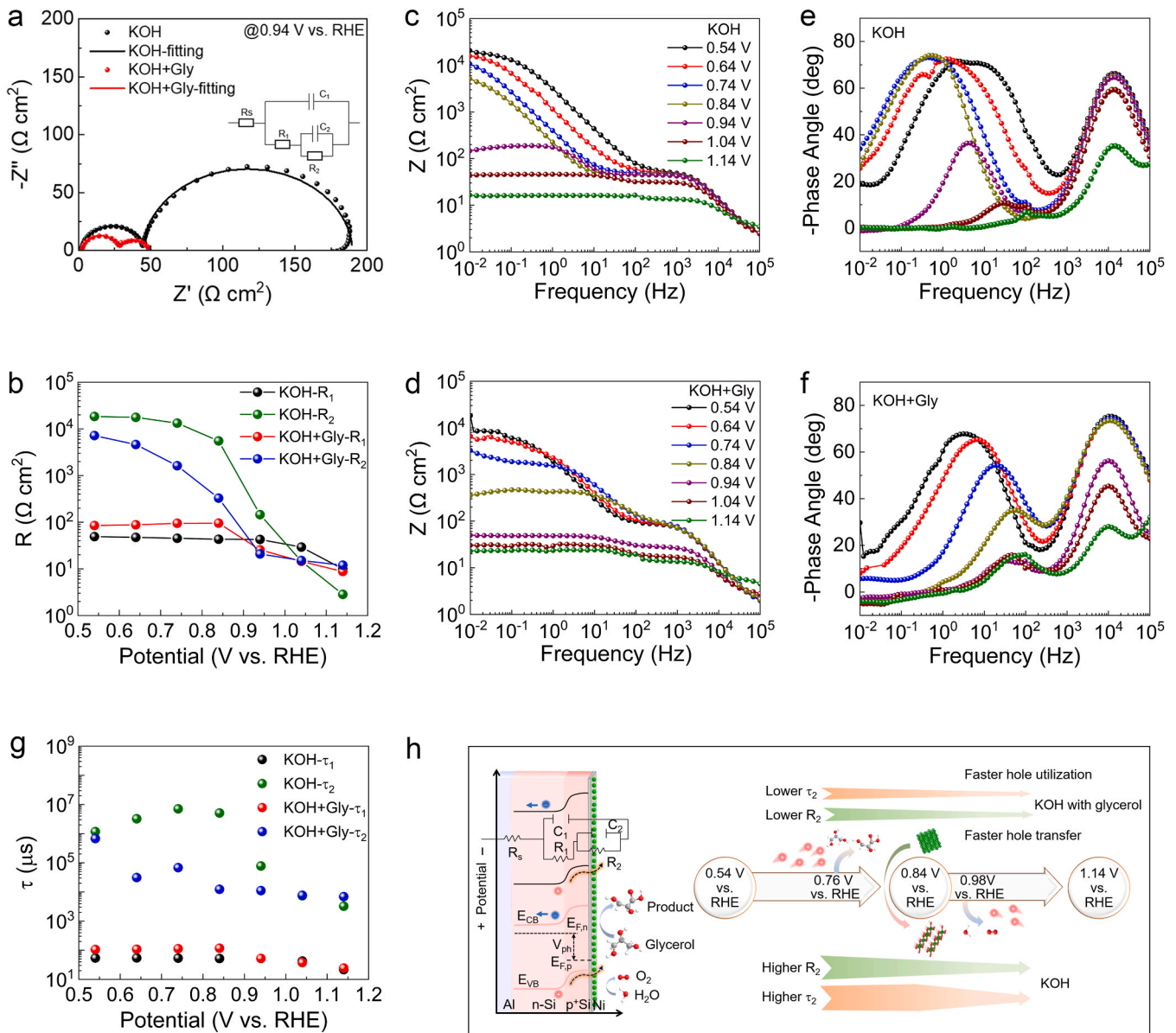

Fig. 5. Charge carrier dynamics. (a) Nyquist plots of the np^+-Si/SiO$_x$/Ni photoanode at 0.94 V (vs. RHE) in 1.0 M KOH with and without 0.1 M glycerol under 1-sun illumination. Inset is the equivalent circuit model. (b) Bulk charge transfer resistance (R_1) and interfacial charge transfer resistance (R_2) as a function of applied potential for OER and GOR. (c-d) Bode plots of the np^+-Si/SiO$_x$/Ni photoanode at various potentials for (c) OER and (d) GOR. (e-f) Bode-phase plots of the np^+-Si/SiO$_x$/Ni photoanode at various potentials for (e) OER and (f) GOR. (g) The carrier lifetime at the bulk solid interface (τ_1) or carrier lifetime at the Ni film/electrolyte interface (τ_2) as a function of applied potential for OER and GOR. (h) Schematic diagram of the reaction process with increasing applied potential.

R$_2$ values). When comparing the R$_2$ values in the two electrolytes (see Fig. 5b and Table S1), it is evident that the addition of glycerol efficiently suppresses the interfacial charge transfer barrier. The smaller R$_2$ values in the presence of glycerol suggest the accelerated transfer kinetics at the photoanode/electrolyte interface, which aligns with the observed performance shown in Fig. 4. At higher potentials (> 0.84 V vs. RHE), a sharp decrease in R$_2$ is observed, and the values even become smaller than R$_1$. This implies that the interfacial charge transfer is no longer the limiting factor at these high potentials. Additionally, R$_1$ gradually decreases after 0.84 V vs. RHE, this potential refers to the oxidation transformation of Ni to NiOOH, which may promote the bulk charge transfer across the photoanode by increasing the barrier height (due to the high work function of NiOOH) [46].

Fig. 5c-d provides detailed Bode plots of the np$^+$-Si/SiO$_x$/Ni photoanode for OER and GOR at various applied potentials. Bode plots offer clear visualization of how the impedance changes with frequency. The low-frequency region ($< 10^2$ Hz) is particularly associated with the interfacial charge transfer process. For the OER, the impedance gradually decreases as the potential shifts from 0.54 to 0.84 V vs. RHE. This decrease in impedance is primarily attributed to the corresponding reduction in R$_2$ (as shown in Fig. 5b and 5c). The decline in R$_2$ suggests an improvement in the charge transfer kinetics from the electrode to the electrolyte. Notably, even more significant decreases in impedance are observed beyond 0.94 V vs. RHE for the OER. This transit potential aligns with the onset potential of the OER observed in Fig. 4b. For the GOR, the impedance is relatively smaller compared to that of the OER at the same potential (Fig. 5d), suggesting that the presence of glycerol greatly promotes the interfacial charge transfer between the electrode and the electrolyte. At the potential of 0.84 V vs. RHE, a sharp decrease in impedance is observed, corresponding to the onset potential of GOR.

In Bode-phase plots, the phase peaks in the high-frequency and low-frequency regions can be used to calculate the lifetime of minority carriers (holes) (Fig. 5e and 5f). The shift of the peak indicates the change of the lifetime for the photogenerated charge carriers. The lifetime of holes before recombination at two interfaces can be calculated based on the following equation: [47,48]

$$\tau_1 = R_1 \times C_1 \tag{2}$$

$$\tau_2 = R_2 \times C_2 \tag{3}$$

In the equation, τ_1 is the carrier lifetime at the bulk solid interface, while τ_2 is the carrier lifetime at the Ni film/electrolyte interface. A smaller τ_1 indicates a faster transfer rate of charge carriers in the bulk photoanode; a smaller τ_2 suggests a more effective charge injection and utilization at the photoanode/electrolyte interface.

The fitted capacitance values were listed and compared in Table S2 and Fig. S8. The calculated values of τ_1 and τ_2 at different potentials in the two electrolytes were provided in Table S3 and the relationship between τ and the applied potential was further illustrated in Fig. 5g. Notably, the value of τ_1 becomes smaller as the applied potential increases, indicating a faster hole transfer rate at high potentials. The value of τ_2 exhibits an interesting trend in KOH, as observed in Fig. 5g. It initially increases and then decreases, corresponding to the shift of the low-frequency peak towards lower frequencies and subsequently towards higher frequencies (Fig. 5e). This can be attributed to the change in reaction rate before and after Ni oxidation, which occurs at around 0.84 V vs. RHE, indicating that the OER starts after oxidation of Ni to NiOOH. On the other hand, in the presence of glycerol (Fig. 5f), the oxidation rate remains elevated even after the formation of NiOOH. This suggests that the glycerol molecule can be directly oxidized by holes without being mediated by NiOOH as the catalyst. In addition, the τ_2 values in the presence of glycerol are substantially smaller compared to those in pure KOH, implying that the holes can be quickly utilized to drive oxidation reactions upon the addition of glycerol. This finding further supports the faster kinetics of GOR.

To gain further insight into the impact of glycerol on the dynamics of charge carriers, the band bending of the np$^+$-Si/SiOx/Ni photoanode in electrolyte was analyzed. The equilibrium state of the metal-insulator-semiconductor (MIS) structure without illumination and bias was illustrated in Fig. S9. In this state, the concentration of charge carriers remains constant at the experimental temperature, and the entire system exhibits a uniform Fermi level. However, when both bias and illumination are applied, the p-n junction transits into a non-equilibrium state, resulting in the appearance of non-equilibrium charge carriers in the internal field region. This phenomenon leads to the separation of the quasi-Fermi levels, as depicted in Fig. 5h. The photovoltage can be defined as the difference between these quasi-Fermi levels, representing the driving force for charge carriers separation and hole transfer [49]. When glycerol is added, the small photovoltage observed in Fig. 4b is in accordance with the large R$_1$ measured in Fig. 5g. However, considering that R$_1$ is not the main influencing factor (due to R$_1 << $ R$_2$ at low potential), thus would have little impact on the overall hole transfer.

Based on the above analysis, the reaction processes occurring at different potentials in the presence or absence of glycerol were summarized in Fig. 5h. The significantly higher R$_2$ values in both electrolytes indicate that the charge transfer at photoanode/electrolyte interface is the primary limiting factor in both oxidation processes. Additionally, distinct differences are observed after addition of glycerol into KOH. Particularly at lower potentials ranging from 0.54 to 0.84 V vs. RHE, the R$_2$ and τ_2 values are significantly smaller compared to those in pure KOH, suggesting faster interfacial charge transfer, more efficient utilization of photogenerated holes, and accelerated reaction rate in the presence of glycerol. At around 0.84 V vs. RHE, Ni (or Ni(OH)$_2$) undergoes oxidation to form NiOOH, which provides active sites for both OER and GOR. After this potential, the values for R$_1$, R$_2$, τ_1, and τ_2 gradually decrease and approach to those observed for OER, indicating that OER and GOR occur simultaneously after reaching this potential.

3.6. Oxidation mechanism of PEC GOR

Generally, the oxidation mechanism of polyols can be classified into two types. One is the direct oxidation, where polyols can be oxidized directly without any significant changes to the catalyst structure. The other one is the indirect oxidation, which involves a structural change in the catalyst followed by the oxidation of polyols through the real active catalyst [50]. To investigate the oxidation mechanism of PEC GOR at the np$^+$-Si/SiO$_x$/Ni photoanode, the LSV profiles for the OER and GOR under illumination were analyzed. Fig. 6a presents a zoomed-in view of these profiles. In the LSV profile obtained in KOH electrolyte, an oxidation peak of Ni was observed at around 0.84 V (vs. RHE). When glycerol was added to the electrolyte, the onset potential for GOR (0.76 V vs. RHE) was observed at a significantly lower potential than the oxidation potential of Ni, suggesting that the oxidation of glycerol takes place before reaching the Ni oxidation potential. This phenomenon implies that glycerol molecules can be directly oxidized by the photogenerated holes without mediating the catalyst transformation, indicating that the PEC GOR process may involve a direct oxidation mechanism.

To deep investigate the direct oxidation mechanism of PEC GOR, LSV profiles were collected with different concentrations of glycerol (see Fig. S10). The relationship between photocurrent density and concentration ratio of glycerol to hydroxyl ions (C$_{Gly}$/C$_{OH}^-$) at various potentials was plotted in Fig. S11. As an example, the relationship at 1.20 V vs. RHE was illustrated in Fig. 6b. Interestingly, a volcano-plot relationship with an optimal glycerol concentration of 0.1 M was observed, further strengthening the evidence for the direct oxidation mechanism during PEC GOR. The concentration-dependent GOR photocurrent is attributed to the competitive adsorption of OH$^-$ and glycerol on the surface of the photoanode.[45] When the C$_{Gly}$/C$_{OH}^-$ ratio is below 0.1, glycerol can be immediately oxidized by holes at the surface rich in OH$^-$, resulting in an increase in the photocurrent density with increasing the proportion of glycerol. When the C$_{Gly}$/C$_{OH}^-$ ratio exceeds 0.1, there is an insufficient
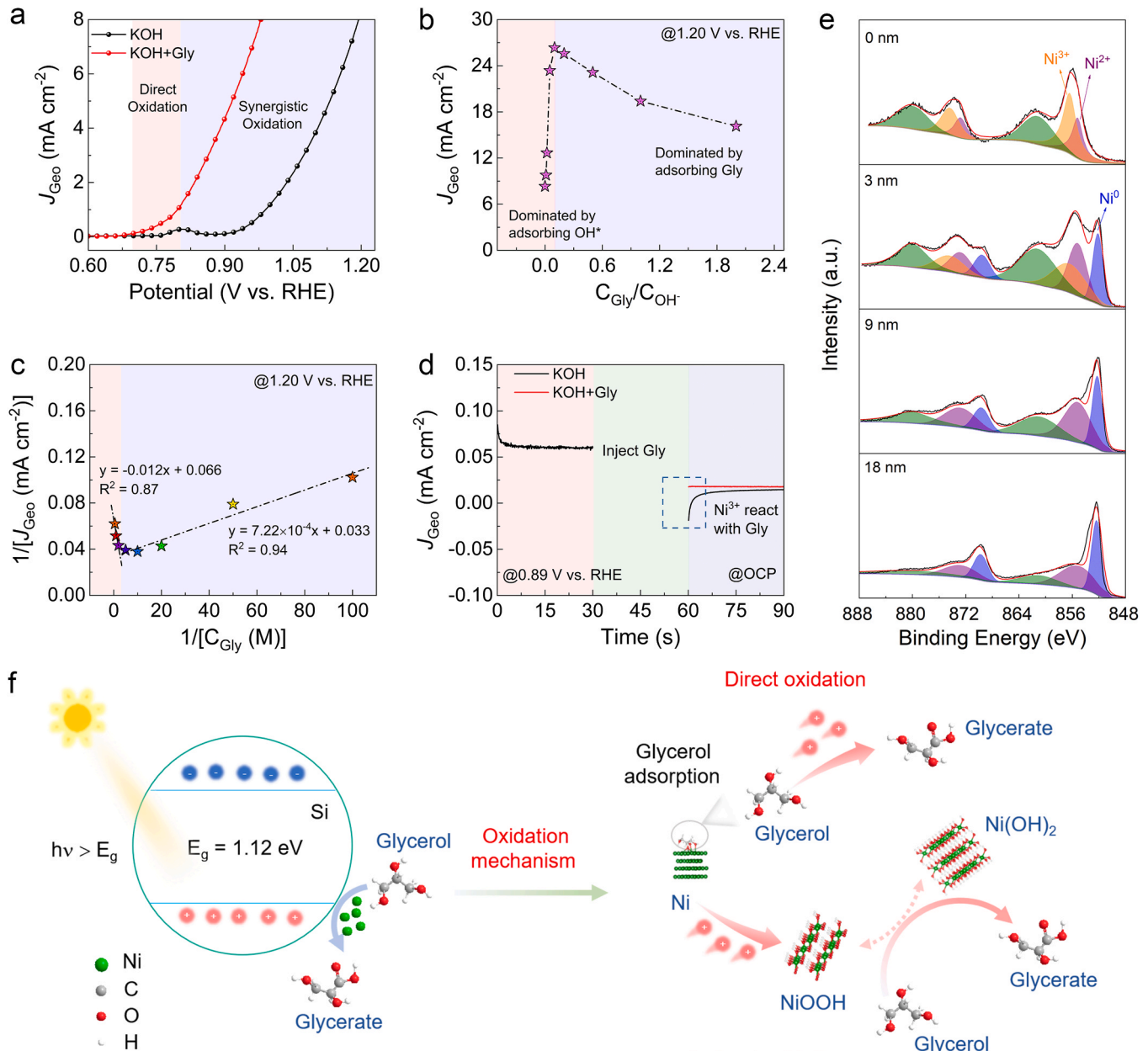
Fig. 6. GOR oxidation mechanism. (a) Zoomed-in LSV profiles of the photoanode in 1.0 M KOH with and without 0.1 M glycerol under 1-sun illumination. (b) Volcano relationship between photocurrent density and C_{Gly}/C_{OH^-} at 1.20 V (vs. RHE). (c) LH linearization between 1/photocurrent density and $1/C_{Gly}$ at 1.20 V (vs. RHE). (d) Multi-potential step curves with and without injection of glycerol. (e) Ni 2p XPS spectra of the post-mortem photoanode upon different ion milling depths. (f) Schematic diagram of the direct and indirect oxidation mechanisms for PEC GOR.

amount of OH$^-$ available to react with the excessive glycerol molecules adsorbed on the photoanode surface. As a result, the photocurrent density decreases as the ratio increases.

Furthermore, based on the unimolecular Langmuir-Hinshelwood (LH) model, where holes are directly trapped by reactants, the reaction rate (r) can be described as follows [51]

$$r = \frac{k_r k_{ads}[S]}{1 + k_{ads}[S]} \qquad (4)$$

A linear relationship can be obtained following:

$$\frac{1}{r} = \frac{1}{k_r} + \frac{1}{[S]} \times \frac{1}{k_r k_{ads}} \qquad (5)$$

where k_r is the reaction constant, k_{ads} is the adsorption constant, $[S]$ is

the glycerol concentration. The reaction rate r is determined by the photocurrent density. By plotting the inverse of the photocurrent density ($\frac{1}{r}$) against the inverse of the concentration of glycerol ($\frac{1}{[S]}$), a linear correlation was observed and illustrated in Fig. 6c. In the low concentration region (0.01 – 0.20 M), the linear fit yielded a coefficient factor (R^2) of 0.94. In the high concentration region (0.50 – 2.00 M), the linear fit resulted in an R^2 of 0.87. These high R^2 values indicate that the data fits well with the unimolecular LH model, supporting the direct oxidation mechanism of PEC GOR.

In addition to the direct oxidation by photogenerated holes, polyols may also undergo indirect oxidation through the participation of catalysts (especially the oxidized species during the metal oxidation process) [52]. To investigate whether there is an indirect oxidation process involved in PEC GOR, a multi-potential step test was performed and the

result was shown in Fig. 6d. Initially, Ni was allowed to oxidize to NiOOH by applying a constant potential of 0.89 V (vs. RHE) under illumination. Subsequently, an open circuit potential (OCP) was applied, a downward reduction current was observed in KOH electrolyte, corresponding to the reduction of Ni^{3+} to Ni^{2+}. However, when glycerol was added, the reduction current vanished, indicating that glycerol has acted as a reducing agent to effectively reduce the generated Ni^{3+} back to Ni^{2+}. This finding suggests that glycerol can be oxidized by NiOOH, implying the presence of an indirect oxidation process involved in PEC GOR.

To further confirm the indirect oxidation mechanism, a post-mortem np^+-Si/SiO$_x$/Ni photoanode was characterized by XPS depth profiling experiments, see Fig. 6e. The XPS analysis revealed the coexistence of Ni^{2+} and Ni^{3+} valence states on the surface of the photoanode. The presence of Ni^{3+} states can be attributed to the oxidized NiOOH species, which can be further supported by the O 2p XPS result (Fig. S12). The difference of Ni 2p XPS spectra before and after GOR indicated a structural transformation of the Ni catalyst during PEC GOR, providing additional evidence for the indirect oxidation mechanism. Interestingly, the proportion of Ni^{3+} gradually decreased to 0 at a depth of approximately 9 nm. Below this depth, the photoanode primarily consisted of metallic Ni, indicating that the oxidation of Ni occurs predominantly in the outer layer with a thickness of around 9 nm.

Based on the above analysis, the oxidation mechanisms involved in PEC GOR at the np^+-Si/SiO$_x$/Ni photoanode were schematically summarized in Fig. 6f. Before reaching a potential of 0.84 V vs. RHE (Ni oxidation potential), PEC GOR predominantly follows a direct oxidation mechanism. At these lower potentials, the illuminated Si generates holes that directly oxidize the adsorbed glycerol molecules on the surface of the photoanode. This direct oxidation occurs without significant changes to the Ni surface. However, once the potential surpasses the Ni oxidation potential, there is a synergistic oxidation mechanism involving both direct and indirect oxidation processes. The direct oxidation process continues alongside the formation of NiOOH species, which can further participate in the oxidation of glycerol to valuable products, while concurrently undergoing reduction from Ni^{3+} back to Ni^{2+}.

3.7. Self-powered PEC polyols oxidation system

In addition to glycerol, other active polyols, such as ethylene glycol and 1,2-propylene glycol have also shown the ability to enhance the hole injection and utilization at the photoanode/electrolyte interface (Fig. S13). Fig. 7a-c provide comparisons of the PEC performance in the presence of 1,2-propylene glycol, ethylene glycol, and glycerol molecules, as compared with pure KOH. The pH values of the electrolyte with different polyols were listed in Table S4, and the pH influence was considered when comparing the performance. The current densities of the np^+-Si/SiO$_x$/Ni photoanode for oxidation of water, 1,2-propylene glycol, ethylene glycol, and glycerol at a potential of 1.23 V vs. RHE were measured to be 9.05, 18.25, 21.74, and 29.89 mA cm^{-2}, respectively (Fig. 7a). The observed high current density in the electrolyte
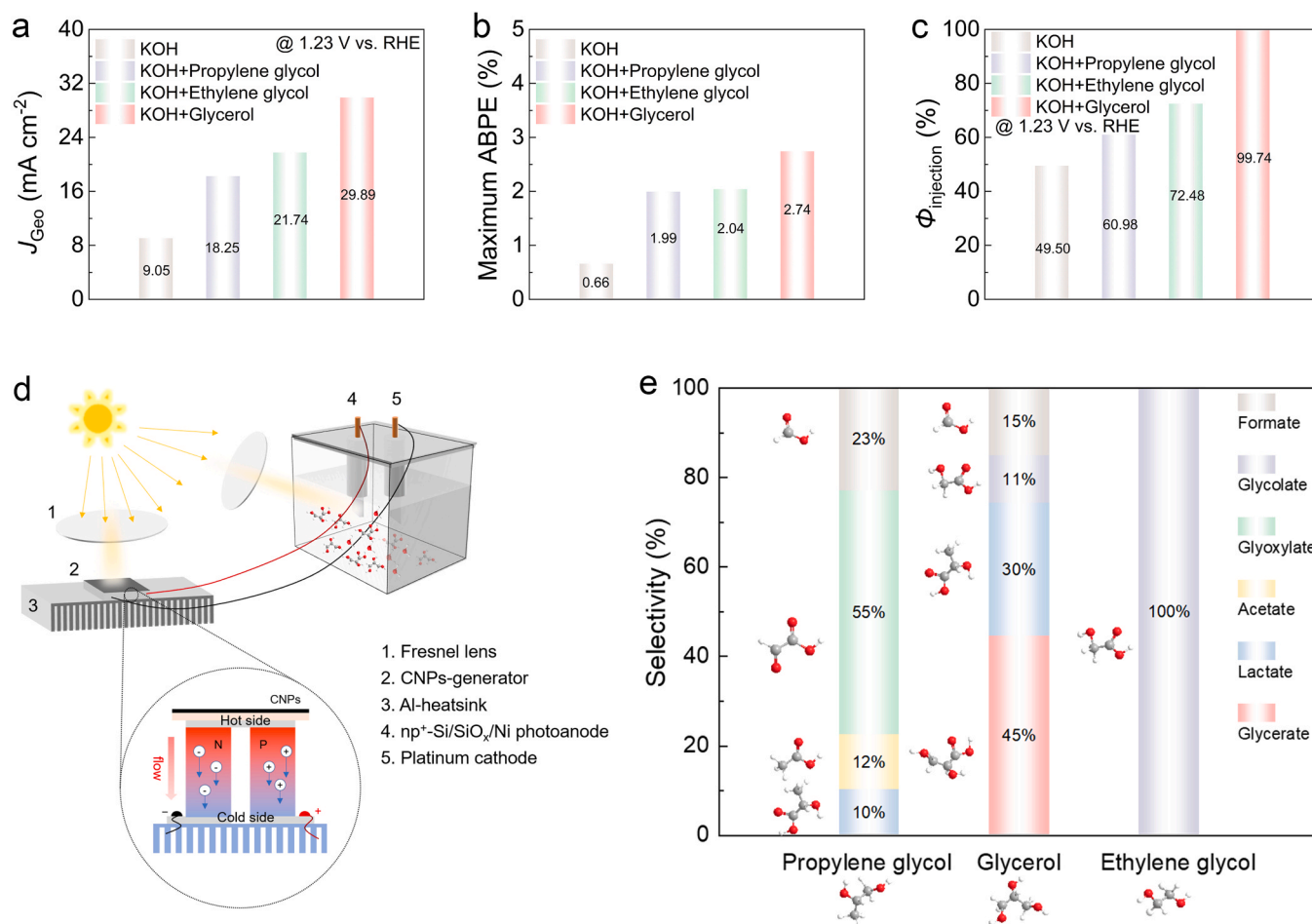

Fig. 7. PEC oxidation performance of different polyols. (a) Comparison of current density at 1.23 V (vs. RHE). (b) Maximum ABPE and (c) $\Phi_{injection}$ (at 1.23 V vs. RHE) of the np^+-Si/SiO$_x$/Ni photoanode for oxidation of H$_2$O, 1,2-propylene glycol, ethylene glycol, and glycerol in a three-electrode PEC cell. (d) Schematic illustration of the two-electrode self-powered PEC system for polyol oxidation. (e) Product distribution from the oxidation of 1,2-propylene glycol, glycerol, and ethylene glycol in a two-electrode self-powered PEC system.

containing polyols suggests that the addition of polyols is beneficial for reducing the recombination of charge carriers and enhancing the utilization of photogenerated holes. The maximum values of ABPE in the presence of 1,2-propylene glycol, ethylene glycol, and glycerol are 1.99%, 2.04%, and 2.74%, respectively, which are increased by 3.01, 3.09, and 4.15 factors than that in pure KOH (0.66%) (Fig. 7b and S14). This indicates an improved photo-electron conversion efficiency in the presence of polyols. Correspondingly, the $\Phi_{injection}$ of the photoanode at 1.23 V vs. RHE is calculated to be 60.98% for 1,2-propylene glycol, 72.48% for ethylene glycol, and 99.74% for glycerol. These values are increased by 23%, 46%, and 101% respectively compared to that in pure KOH electrolyte (Fig. 7c). The above results indicate that polyol molecules contribute to higher power conversion efficiencies due to the improved hole injection and utilization at the photoanode/electrolyte interface.

To examine the potential application of the PEC system with the np$^+$-Si/SiO$_x$/Ni photoanode, we integrated a STEG with the PEC cell. This configuration allowed us to harness electricity from sunlight and utilize it for the oxidation of polyols. The STEG device was constructed by linking the cold side of the thermoelectric generator to an aluminum heatsink using thermal silicone grease. While the hot side that had been modified with CNPs was exposed on the top for solar illumination (see details in the Experimental Section). The heat required for the operation of the STEG was generated by focusing the sunlight with a Fresnel lens [53]. The schematic illustration of the PEC cell with a STEG was depicted in Fig. 7d. The polyol oxidation process in a PEC cell was conducted in a two-electrode configuration. Under light illumination, the np$^+$-Si/SiO$_x$/Ni photoanode generated holes that facilitate the oxidation reaction, while a Pt slice served as the cathode to receive electrons for the hydrogen evolution reaction. The STEG device was connected with both the photoanode and cathode to provide additional electricity required for the whole reaction. To ensure result reproducibility, a Xenon lamp was used as a sunlight simulator, enabling the STEG device to generate a voltage of approximately 1.21 V (Fig. S15).

In this self-powered PEC system, the resulting products from the oxidation of 1,2-propylene glycol, glycerol, and ethylene glycol were collected after 1 h operation and then quantitatively analyzed by HPLC (see Fig. 7e). The dominant product from the oxidation of 1,2-propylene glycol is glyoxylate, with a selectivity of 55%. The process involves the initial oxidation of the primary hydroxyl group to result in lactate, which then further converts into glyoxylate through C-C bond cleavage (Fig. S16). The glyoxylate can be widely used as the intermediates for pharmaceuticals, chemical additives, and cosmetics [54]. Furthermore, the main product obtained from the oxidation of glycerol is glycerate, with a selectivity of 45%. This suggests that the conversion of glycerol involves the continuous oxidation of its primary hydroxyl group, mediating from glyceraldehyde and finally progressing to glycerate (Fig. S17) [55]. In addition to glycerate, lactate can also be produced from the oxidation of glycerol with a selectivity of 30%. It probably originates from the oxidation of the secondary hydroxyl group of glycerol, proceeding through 1,2 dihydroxyacetone and subsequent removal of one molecule of water. The resulting compound then undergoes Cannizzaro rearrangement to form lactate [56,57]. It is worth noting that the selectivity towards C3 products from the PEC oxidation of glycerol is as high as 75%, which is rarely reported for non-noble metal catalysts especially in alkaline media. Glycerate is a useful chemical compound with various applications in the food and medicine industries [58]. Lactate can be used as the souring, antibacterial, and moisturzing agents. The only detected product from the oxidation of ethylene glycol is glycolate, suggesting that it comes from the continuous oxidation of the same hydroxyl group of ethylene glycol [59]. This process proceeds through glycolaldehyde and eventually forms glycolate in the alkaline media (Fig. S18). Glycolate can be used as the degreasing agent, textile dyeing, and leather tanning agent [58]. The results discussed above showcase the promising potential of this self-powered PEC system for transforming low-cost biomass polyols into valuable products solely relying on renewable solar energy.

4. Conclusion

In summary, we successfully synthesized the np$^+$-Si/SiO$_x$/Ni photoanode *via* microfabrication process and a facile electrodeposition method. We innovatively introduced energetically favorable polyol molecules (such as glycerol, 1,2-propylene glycol, and ethylene glycol) into the alkaline electrolyte for a Si-based PEC oxidation system. The introduction of polyols, particularly glycerol, greatly enhanced the PEC performance of the Si photoanode, resulting in an impressively low onset potential of 0.76 V vs. RHE, which was reduced by 0.22 V compared to pure KOH electrolyte. Additionally, the maximum ABPE increased 4-fold and the injection efficiency increased by 101% (at 1.23 V vs. RHE) in the presence of glycerol. *In-situ* EIS spectra confirmed the accelerated hole transfer and utilization at the photoanode/electrolyte interface when glycerol was present. Furthermore, the oxidation mechanism of PEC GOR was deeply studied, revealing that the glycerol was directly oxidized by photogenerated holes at lower potentials and underwent synergistic oxidation process mediated by holes and catalysts at higher potentials. Finally, we designed a self-powered PEC system for polyol oxidation, demonstrating the practical feasibility of converting low-cost biomass alcohols into value-added products solely relying on renewable solar energy.

CRediT authorship contribution statement

Yaxing Zhao: Writing – review & editing, Writing – original draft, Formal analysis, Data curation. **Xuedong Zhang:** Software. **Yuanhua Sang:** Funding acquisition. **Xiaowen Yu:** Writing – review & editing, Funding acquisition. **Hong Liu:** Writing – review & editing. **Xiaolei Zhao:** Conceptualization. **Kepeng Song:** Software. **Xiaowen Sun:** Resources. **Ning Xi:** Investigation.

Declaration of Competing Interest

The authors declare that they have no known competing financial interests or personal relationships that could have appeared to influence the work reported in this paper.

Data availability

Data will be made available on request.

Appendix A. Supporting information

Supplementary data associated with this article can be found in the online version at doi:10.1016/j.apcatb.2024.123901.

References

[1] S. Wang, G. Liu, L. Wang, Crystal facet engineering of photoelectrodes for photoelectrochemical water splitting, Chem. Rev. 119 (2019) 5192–5247, https://doi.org/10.1021/acs.chemrev.8b00584.

[2] B. Liu, S. Wang, G. Zhang, Z. Gong, B. Wu, T. Wang, J. Gong, Tandem cells for unbiased photoelectrochemical water splitting, Chem. Soc. Rev. 52 (2023) 4644–4671, https://doi.org/10.1039/d3cs00145h.

[3] X.M.C. Ta, R. Daiyan, T.K.A. Nguyen, R. Amal, T. Tran-Phu, A. Tricoli, Alternatives to water photooxidation for photoelectrochemical solar energy conversion and

green H$_2$ production, Adv. Energy Mater. 12 (2022) 2201358, https://doi.org/10.1002/aenm.202201358.

[4] A. Fujishima, K. Honda, Electrochemical photolysis of water at a semiconductor electrode, Nature 238 (1972) 37–38, https://doi.org/10.1038/238037a0.

[5] Y. Wang, W. Tian, C. Chen, W. Xu, L. Li, Tungsten trioxide nanostructures for photoelectrochemical water splitting: material engineering and charge carrier dynamic manipulation, Adv. Funct. Mater. 29 (2019) 1809036, https://doi.org/10.1002/adfm.201809036.

[6] D. Liu, J.C. Liu, W. Cai, J. Ma, H.B. Yang, H. Xiao, J. Li, Y. Xiong, Y. Huang, B. Liu, Selective photoelectrochemical oxidation of glycerol to high value-added dihydroxyacetone, Nat. Commun. 10 (2019) 1779, https://doi.org/10.1038/s41467-019-09788-5.

[7] X. Wang, B. Liu, Y. Zhang, T. Butburee, K. Ostrikov, S. Wang, W. Huang, Development of ABO$_4$-type photoanodes for photoelectrochemical water splitting, EcoEnergy 1 (2023) 108–153, https://doi.org/10.1002/ece2.11.

[8] J.W. Yang, I.J. Park, S.A. Lee, M.G. Lee, T.H. Lee, H. Park, C. Kim, J. Park, J. Moon, J.Y. Kim, H.W. Jang, Near-complete charge separation in tailored BiVO$_4$-based heterostructure photoanodes toward artificial leaf, Appl. Catal. B: Environ. 293 (2021) 120217, https://doi.org/10.1016/j.apcatb.2021.120217.

[9] S. Yuan, L. Jiang, J. Hu, H. Liu, J. Wang, Fully dispersed IrOx atomic clusters enable record photoelectrochemical water oxidation of hematite in acidic media, Nano Lett. 23 (2023) 2354–2361, https://doi.org/10.1021/acs.nanolett.3c00245.

[10] D.H. Nam, G.M. Ryu, S.K. Kuk, D.S. Choi, E.J. Son, C.B. Park, Water oxidation-coupled, photoelectrochemical redox biocatalysis toward mimicking natural photosynthesis, Appl. Catal. B: Environ. 198 (2016) 311–317, https://doi.org/10.1016/j.apcatb.2016.05.077.

[11] J. Ma, H. Chi, A. Wang, P. Wang, H. Jing, T. Yao, C. Li, Identifying and removing the interfacial states in metal-oxide-semiconductor schottky Si photoanodes for the highest fill factor, J. Am. Chem. Soc. 144 (2022) 17540–17548, https://doi.org/10.1021/jacs.2c06748.

[12] W. Jin, C. Shin, S. Lim, K. Lee, J.M. Yu, K. Seo, J.-W. Jang, Natural leaf-inspired solar water splitting system, Appl. Catal. B: Environ. 322 (2023) 122086, https://doi.org/10.1016/j.apcatb.2022.122086.

[13] R. Yang, Y. Ji, Q. Li, Z. Zhao, R. Zhang, L. Liang, F. Liu, Y. Chen, S. Han, X. Yu, H. Liu, Ultrafine Si nanowires/Sn$_3$O$_4$ nanosheets 3D hierarchical heterostructured array as a photoanode with high-efficient photoelectrocatalytic performance, Appl. Catal. B: Environ. 256 (2019) 117798, https://doi.org/10.1016/j.apcatb.2019.117798.

[14] K. Sun, S. Shen, Y. Liang, P.E. Burrows, S.S. Mao, D. Wang, Enabling silicon for solar-fuel production, Chem. Rev. 114 (2014) 8662–8719, https://doi.org/10.1021/cr300459q.

[15] K. Aoki, K. Ishiguro, M. Denokami, Y. Tanahashi, K. Furusawa, N. Sekine, T. Adschiri, M. Fujii, Direct microrolling processing on a silicon wafer, Small 13 (2017) 1701630, https://doi.org/10.1002/smll.201701630.

[16] Z. Luo, T. Wang, J. Gong, Single-crystal silicon-based electrodes for unbiased solar water splitting: current status and prospects, Chem. Soc. Rev. 48 (2019) 2158–2181, https://doi.org/10.1039/c8cs00638e.

[17] D. Bae, B. Seger, P.C.K. Vesborg, O. Hansen, I. Chorkendorff, Strategies for stable water splitting via protected photoelectrodes, Chem. Soc. Rev. 46 (2017) 1933–1954, https://doi.org/10.1039/c6cs00918b.

[18] Y.W. Chen, J.D. Prange, S. Duhnen, Y. Park, M. Gunji, C.E.D. Chidsey, P. C. McIntyre, Atomic layer-deposited tunnel oxide stabilizes silicon photoanodes for water oxidation, Nat. Mater. 10 (2011) 539–544, https://doi.org/10.1038/nmat3047.

[19] H.J. Fu, P. Buabthong, Z.P. Ifkovits, W. Yu, B.S. Brunschwig, N.S. Lewis, Catalytic open-circuit passivation by thin metal oxide films of p-Si anodes in aqueous alkaline electrolytes, Energy Environ. Sci. 15 (2022) 334–345, https://doi.org/10.1039/d1ee03040j.

[20] M.J. Kenney, M. Gong, Y. Li, J.Z. Wu, J. Feng, M. Lanza, H. Dai, High-performance silicon photoanodes passivated with ultrathin nickel films for water oxidation, Science 342 (2013) 836–840, https://doi.org/10.1126/science.1241327.

[21] X.H. Zhou, R. Liu, K. Sun, K.M. Papadantonakis, B.S. Brunschwig, N.S. Lewis, 570 mV photovoltage, stabilized n-Si/CoOx heterojunction photoanodes fabricated using atomic layer deposition, Energy Environ. Sci. 9 (2016) 892–897, https://doi.org/10.1039/c5ee03655k.

[22] C. Deng, C.Y. Toe, X. Li, J. Tan, H. Yang, Q. Hu, C. He, Earth-abundant metal-based electrocatalysts promoted anodic reaction in hybrid water electrolysis for efficient hydrogen production: recent progress and perspectives, Adv. Energy Mater. 12 (2022) 2201047, https://doi.org/10.1002/aenm.202201047.

[23] B. Liu, S. Feng, L. Yang, C. Li, Z. Luo, T. Wang, J. Gong, Bifacial passivation of n-silicon metal–insulator–semiconductor photoelectrodes for efficient oxygen and hydrogen evolution reactions, Energy Environ. Sci. 13 (2020) 221–228, https://doi.org/10.1039/c9ee02766a.

[24] F.A.L. Laskowski, S.Z. Oener, M.R. Nellist, A.M. Gordon, D.C. Bain, J.L. Fehrs, S. W. Boettcher, Nanoscale semiconductor/catalyst interfaces in photoelectrochemistry, Nat. Mater. 19 (2019) 69–76, https://doi.org/10.1038/s41563-019-0488-z.

[25] Y. Li, G. Xu, X. Zhu, Z. Man, X. Fu, Z. Hao, Y. Cui, C. Yuan, W. Zhang, S. Yan, H. Ge, Y. Chen, Z. Zou, A hierarchical dual-phase photoetching template route to assembling functional layers on Si photoanode with tunable nanostructures for efficient water splitting, Appl. Catal. B: Environ. 259 (2019) 118115, https://doi.org/10.1016/j.apcatb.2019.118115.

[26] J.C. Hill, A.T. Landers, J.A. Switzer, An electrodeposited inhomogeneous metal-insulator-semiconductor junction for efficient photoelectrochemical water oxidation, Nat. Mater. 14 (2015) 1150–1155, https://doi.org/10.1038/nmat4408.

[27] Z. Luo, B. Liu, H. Li, X. Chang, W. Zhu, T. Wang, J. Gong, Multifunctional nickel film protected n-type silicon photoanode with high photovoltage for efficient and stable oxygen evolution reaction, Small Methods 3 (2019) 1900212, https://doi.org/10.1002/smtd.201900212.

[28] T. Han, Y. Shi, Z. Yu, B. Shin, M. Lanza, Potassium hydroxide mixed with lithium hydroxide: an advanced electrolyte for oxygen evolution reaction, Sol. RRL 3 (2019) 1900195, https://doi.org/10.1002/solr.201900195.

[29] X.W. Yu, P. Yang, S. Chen, M. Zhang, G.Q. Shi, NiFe alloy protected silicon photoanode for efficient water splitting, Adv. Energy Mater. 7 (2017) 1601805, https://doi.org/10.1002/aenm.201601805.

[30] P. Pál, M. Veres, R. Holomb, M. Szalóki, A.G. Szöllősi, I. Csarnovics, Identification of histidine-Ni (II) metal complex by Raman spectroscopy, J. Raman Spectrosc. 54 (2022) 278–287, https://doi.org/10.1002/jrs.6490.

[31] N.S. Biradar, B.R. Patil, V.H. Kulkarni, Transformation of square-planar dsp^2 configuration of Ni(II) aldoximes into octahedral sp^{3}d^2 configuration by reaction with Tin(IV) chloride, J. Inorg. Nucl. Chem. 37 (1975) 1901–1904, https://doi.org/10.1016/0022-1902(75)80911-0.

[32] S. Lee, L. Ji, A.C. De Palma, E.T. Yu, Scalable, highly stable Si-based metal-insulator-semiconductor photoanodes for water oxidation fabricated using thin-film reactions and electrodeposition, Nat. Commun. 12 (2021) 3982, https://doi.org/10.1038/s41467-021-24229-y.

[33] S.E. Jun, Y.-H. Kim, J. Kim, W.S. Cheon, S. Choi, J. Yang, H. Park, H. Lee, S.H. Park, K.C. Kwon, J. Moon, S.-H. Kim, H.W. Jang, Atomically dispersed iridium catalysts on silicon photoanode for efficient photoelectrochemical water splitting, 609-609, Nat. Commun. 14 (2023), https://doi.org/10.1038/s41467-023-36335-0.

[34] G.C. Xie, B.D. Guo, J.R. Gong, Metal oxide/graphene/metal sandwich structure for efficient photoelectrochemical water oxidation, Adv. Funct. Mater. 33 (2023) 2210420, https://doi.org/10.1002/adfm.202210420.

[35] Y. Li, X. Wei, L. Chen, J. Shi, M. He, Nickel-molybdenum nitride nanoplate electrocatalysts for concurrent electrolytic hydrogen and formate productions, Nat. Commun. 10 (2019) 5335, https://doi.org/10.1038/s41467-019-13375-z.

[36] J. Zhao, T.M. Gill, X. Zheng, Enabling silicon photoanodes for efficient solar water splitting by electroless-deposited nickel, Nano Res. 11 (2018) 3499–3508, https://doi.org/10.1007/s12274-018-2038-4.

[37] F. Wu, Q. Liao, F. Cao, L. Li, Y. Zhang, Non-noble bimetallic NiMoO$_4$ nanosheets integrated Si photoanodes for highly efficient and stable solar water splitting, Nano Energy 34 (2017) 8–14, https://doi.org/10.1016/j.nanoen.2017.02.004.

[38] I.A. Digdaya, G.W.P. Adhyaksa, B.J. Trzesniewski, E.C. Garnett, W.A. Smith, Interfacial engineering of metal-insulator-semiconductor junctions for efficient and stable photoelectrochemical water oxidation, Nat. Commun. 8 (2017) 15968, https://doi.org/10.1038/ncomms15968.

[39] A.G. Scheuermann, J.P. Lawrence, K.W. Kemp, T. Ito, A. Walsh, C.E.D. Chidsey, P. K. Hurley, P.C. McIntyre, Design principles for maximizing photovoltage in metal-oxide-protected water-splitting photoanodes, Nat. Mater. 15 (2016) 99–105, https://doi.org/10.1038/nmat4451.

[40] T. Yao, R. Chen, J. Li, J. Han, W. Qin, H. Wang, J. Shi, F. Fan, C. Li, Manipulating the interfacial energetics of n-type silicon photoanode for efficient water oxidation, J. Am. Chem. Soc. 138 (2016) 13664–13672, https://doi.org/10.1021/jacs.6b07188.

[41] C.R. Jiang, S.J.A. Moniz, A.Q. Wang, T. Zhang, J.W. Tang, Photoelectrochemical devices for solar water splitting-materials and challenges, Chem. Soc. Rev. 46 (2017) 4645–4660, https://doi.org/10.1039/c6cs00306k.

[42] S.A. Lee, J.W. Yang, T.H. Lee, I.J. Park, C. Kim, H. Lee, S. Choi, J. Moon, S.Y. Kim, J.Y. Kim, H.W. Jang, Multifunctional nano-heterogeneous Ni(OH)$_2$/NiFe catalysts on silicon photoanode toward efficient water and urea oxidation, Appl. Catal. B: Environ. 317 (2022) 121765, https://doi.org/10.1016/j.apcatb.2022.121765.

[43] Y. Miao, J. Liu, L. Chen, H. Sun, R. Zhang, J. Guo, M. Shao, Single-atomic-Co cocatalyst on (040) facet of BiVO$_4$ toward efficient photoelectrochemical water splitting, Chem. Eng. J. 427 (2022) 131011, https://doi.org/10.1016/j.cej.2021.131011.

[44] Q. Cai, W. Hong, C. Jian, J. Li, W. Liu, Insulator layer engineering toward stable Si photoanode for efficient water oxidation, ACS Catal. 8 (2018) 9238–9244, https://doi.org/10.1021/acscatal.8b01398.

[45] Q. Wang, J.-E. Moser, M. Grätzel, Electrochemical impedance spectroscopic analysis of dye-sensitized solar cells, J. Phys. Chem. B 109 (2005) 14945–14953, https://doi.org/10.1021/jp052768h.

[46] Q. Cai, W. Hong, C. Jian, W. Liu, A high-performance silicon photoanode enabled by oxygen vacancy modulation on NiOOH electrocatalyst for water oxidation, Nanoscale 12 (2020) 7550–7556, https://doi.org/10.1039/d0nr00921k.

[47] S. Elnobi, M. Dongol, T. Soga, A.A. Abuelwafa, Charge transport, photoresponse and impedance spectroscopy for Au/NiTPP/n-Si/Al diode, J. Alloy. Compd. 965 (2023) 171235, https://doi.org/10.1016/j.jallcom.2023.171235.

[48] D. Wang, J. Zhu, L. Ding, P. Gao, X. Pan, J. Sheng, J. Ye, Interface electric properties of Si/organic hybrid solar cells using impedance spectroscopy analysis, Jpn. J. Appl. Phys. 55 (2016) 056601, https://doi.org/10.7567/jjap.55.056601.

[49] I.A. Digdaya, B.J. Trześniewski, G.W.P. Adhyaksa, E.C. Garnett, W.A. Smith, General considerations for improving photovoltage in metal–insulator–semiconductor photoanodes, J. Phys. Chem. C 122 (2018) 5462–5471, https://doi.org/10.1021/acs.jpcc.7b11747.

[50] Y. Lu, T. Liu, Y.-C. Huang, L. Zhou, Y. Li, W. Chen, L. Yang, B. Zhou, Y. Wu, Z. Kong, Z. Huang, Y. Li, C.-L. Dong, S. Wang, Y. Zou, Integrated catalytic sites for highly efficient electrochemical oxidation of the aldehyde and hydroxyl groups in 5-hydroxymethylfurfural, ACS Catal. 12 (2022) 4242–4251, https://doi.org/10.1021/acscatal.2c00174.

[51] M.I. Jaramillo-Gutiérrez, J.S. Velasco-Rueda, J.A. Pedraza-Avella, Kinetic approach by photocurrent measurements to the photoelectrocatalytic oxidation of an anionic

surfactant using an S,N-TiO$_2$/Ti electrode: distinguishing between direct and indirect mechanisms, Top. Catal. 64 (2021) 26–35, https://doi.org/10.1007/s11244-020-01404-x.

[52] W. Chen, C. Xie, Y. Wang, Y. Zou, C.-L. Dong, Y.-C. Huang, Z. Xiao, Z. Wei, S. Du, C. Chen, B. Zhou, J. Ma, S. Wang, Activity origins and design principles of nickel-based catalysts for nucleophile electrooxidation, Chem 6 (2020) 2974–2993, https://doi.org/10.1016/j.chempr.2020.07.022.

[53] X. Zhang, W. Gao, X. Su, F. Wang, B. Liu, J.-J. Wang, H. Liu, Y. Sang, Conversion of solar power to chemical energy based on carbon nanoparticle modified photo-thermoelectric generator and electrochemical water splitting system, Nano Energy 48 (2018) 481–488, https://doi.org/10.1016/j.nanoen.2018.03.055.

[54] J. Wu, X. Yang, M. Gong, Recent advances in glycerol valorization via electrooxidation: catalyst, mechanism and device, Chin. J. Catal. 43 (2022) 2966–2986, https://doi.org/10.1016/s1872-2067(22)64121-4.

[55] X. Yu, R.B. Araujo, Z. Qiu, E. Campos dos Santos, A. Anil, A. Cornell, L.G. M. Pettersson, M. Johnsson, Hydrogen evolution linked to selective oxidation of glycerol over CoMoO$_4$—a theoretically predicted catalyst, Adv. Energy Mater. 12 (2022) 2103750, https://doi.org/10.1002/aenm.202103750.

[56] X. Yu, E.C. dos Santos, J. White, G. Salazar-Alvarez, L.G.M. Pettersson, A. Cornell, M. Johnsson, Electrocatalytic glycerol oxidation with concurrent hydrogen evolution utilizing an efficient MoOx/Pt catalyst, Small 17 (2021) 2104288, https://doi.org/10.1002/smll.202104288.

[57] N. Xi, Y. Zang, X. Sun, J. Yu, M. Johnsson, Y. Dai, Y. Sang, H. Liu, X. Yu, Polyhedral coordination determined Co-O activity for electrochemical oxidation of biomass alcohols, Adv. Energy Mater. 13 (2023) 2301572, https://doi.org/10.1002/aenm.202301572.

[58] G. Dodekatos, S. Schünemann, H. Tüysüz, Recent advances in thermo-, photo-, and electrocatalytic glycerol oxidation, ACS Catal. 8 (2018) 6301–6333, https://doi.org/10.1021/acscatal.8b01317.

[59] D. Si, B. Xiong, L. Chen, J. Shi, Highly selective and efficient electrocatalytic synthesis of glycolic acid in coupling with hydrogen evolution, Chem. Catal. 1 (2021) 941–955, https://doi.org/10.1016/j.checat.2021.08.001.